APL Machine Learning

RESEARCH ARTICLE | MAY 26 2023

Designing composition ratio of magnetic alloy multilayer for transverse thermoelectric conversion by Bayesian optimization

Naoki Chiba; Keisuke Masuda; Ken-ichi Uchida; ... et. al

APL Machine Learning 1, 026114 (2023)
https://doi.org/10.1063/5.0140332

AIP Publishing

Designing composition ratio of magnetic alloy multilayer for transverse thermoelectric conversion by Bayesian optimization

Cite as: APL Mach. Learn. 1, 026114 (2023); doi: 10.1063/5.0140332
Submitted: 28 December 2022 • Accepted: 13 April 2023 •
Published Online: 26 May 2023

Naoki Chiba[1,2] Keisuke Masuda[1] Ken-ichi Uchida[1,2,3] and Yoshio Miura[1,4,a)]

AFFILIATIONS

[1] Research Center for Magnetic and Spintronic Materials, National Institute for Materials Science, Tsukuba 305-0047, Japan
[2] Department of Mechanical Engineering, The University of Tokyo, Tokyo 113-8656, Japan
[3] Institute for Materials Research, Tohoku University, Sendai 980-8577, Japan
[4] Center for Spintronics Research Network, Osaka University, Osaka 560-8531, Japan

[a)] **Author to whom correspondence should be addressed:** MIURA.Yoshio@nims.go.jp

ABSTRACT

We demonstrated the effectiveness of the machine learning method combined with first-principles calculations for the enhancement of the anomalous Nernst effect (ANE) of multilayers. The composition ratio of CoNi homogeneous alloy superlattices was optimized by Bayesian optimization so as to maximize the transverse thermoelectric conductivity (α_{xy}). The nonintuitive optimal composition with a large α_{xy} of ~10 A K^{-1} m^{-1} was identified through the two-step Bayesian optimization using rough and fine candidate pools. The Berry curvature and band dispersion analyses revealed that α_{xy} is enhanced by the appearance of the flat band near the Fermi level due to the multilayer formation. The magnitude of the energy derivative of the anomalous Hall conductivity increases owing to the large Berry curvature near the flat band along the R-M high symmetry line, which emerges only in the optimized superlattice, leading to the α_{xy} enhancement. The effective method verified here will broaden the choices of ANE materials to more complex systems and, therefore, lead to the development of transverse thermoelectric conversion technologies.

I. INTRODUCTION

Spin caloritronics,[1–3] the research field based on the combination of spintronics and thermoelectrics, has attracted much attention from the viewpoints of both academic interest and applications. The discovery of the spin Seebeck effect,[4–7] which refers to the spin voltage generation from a temperature gradient, explosively expanded spin caloritronics owing to its unique functionalities, such as thermoelectric generation using insulators.[5] In addition to such a thermo-spin effect, thermoelectric conversion phenomena in magnetic materials, such as magneto-Seebeck[8–10] and magneto-Peltier effects,[11–13] have subsequently stimulated the renewed interest of many researchers. Another typical thermoelectric effect in magnetic materials is the anomalous Nernst effect (ANE),[14–32] where an electric field $\mathbf{E}_{\mathrm{ANE}}$ is generated in the direction perpendicular to both a temperature gradient ∇T and magnetization $\mathbf{M}$ following the relation:

$$\mathbf{E}_{\mathrm{ANE}} = S_{\mathrm{ANE}}\left(\frac{\mathbf{M}}{|\mathbf{M}|}\right) \times \nabla T, \tag{1}$$

where S_{ANE} is the anomalous Nernst coefficient. Thanks to the orthogonal relation between $\mathbf{E}_{\mathrm{ANE}}$ and ∇T, thermoelectric modules based on ANE can increase the output voltage (power) simply by elongating the device length (enlarging the device area) perpendicular to ∇T without forming the number of serial junctions required in the Seebeck-effect-based module. This simple scaling law and device structure make ANE attractive and suitable for thermoelectric conversion applications. However, the currently reported thermopower of ANE, S_{ANE}, is smaller than that of the Seebeck effect by 1–2 orders

of magnitude, which hinders practical applications of the transverse thermoelectric conversion.[33,34]

To improve the thermoelectric conversion performance of ANE, finding and developing materials with large S_{ANE} is essential. The material search guideline for ANE can be clarified by considering two components of S_{ANE} expressed as

$$S_{ANE} = \rho_{xx}\alpha_{xy} + \rho_{xy}\alpha_{xx}, \quad (2)$$

where ρ_{xx} (ρ_{xy}) is the diagonal (off-diagonal) component of the resistivity tensor and α_{xx} (α_{xy}) is the longitudinal (transverse) thermoelectric conductivity. The second term of Eq. (2) originates from the anomalous Hall effect (AHE) induced by the longitudinal carrier flow driven by the Seebeck effect. In contrast, the first term of Eq. (2) represents the intrinsic generation of a transverse electric field from α_{xy}. Since the second term ($\rho_{xy}\alpha_{xx}$) is often smaller than the first term ($\rho_{xx}\alpha_{xy}$) due to the small AHE angle and/or Seebeck coefficient ($S = \rho_{xx}\alpha_{xx}$) in metallic systems, finding materials with a large α_{xy} is a recent strategy in enhancing S_{ANE}. In addition, materials with large α_{xy} can generate a large transverse charge current and power from ∇T, which makes the first term ($\rho_{xx}\alpha_{xy}$) an important parameter. As the Berry curvature[35] of the electronic bands plays a crucial role for the intrinsic ANE, topological materials such as Co-based Heusler compounds[20,21,25] were reported to show large α_{xy}. The large S_{ANE} and α_{xy} were also observed in $SmCo_5$-type permanent magnets,[23,27] Fe_3Ga,[26] $UCo_{0.8}Ru_{0.2}Al$,[30] and $YbMnBi_2$.[31]

Another important system for ANE is metallic multilayers.[17,18,28] Various combinations of ferromagnetic and nonmagnetic materials show the enhancement of S_{ANE} by changing the stacking structure of the multilayer systems. ANE in metallic multilayers such as Fe/Pt and Co/Pt was observed to increase with increasing interface density.[17,18] Ni/Pt superlattices were also reported to exhibit remarkably enhanced ANE compared to a Ni monolayer.[28] Although the microscopic origins of increased ANE in multilayer systems still remain to be clarified, there are several possible factors, such as proximity-induced magnetism,[36,37] interfacial spin–orbit interaction,[38] and interface alloying.[39] Due to the presence of various tunable parameters, the optimization of multilayer structures for ANE is time-consuming and difficult.

Materials informatics (MI),[40,41] the integration of data science and traditional calculations/experiments for efficient discovery and design of new materials, is one of the possible solutions to this difficulty with the increased number of candidates. MI has succeeded in reducing the computational cost by introducing machine learning methods such as Bayesian optimization and Monte Carlo tree search.[42–51] Therefore, it would be effective to apply MI methods to material search in multilayer systems with a large number of candidates for the enhancement of transverse thermoelectric

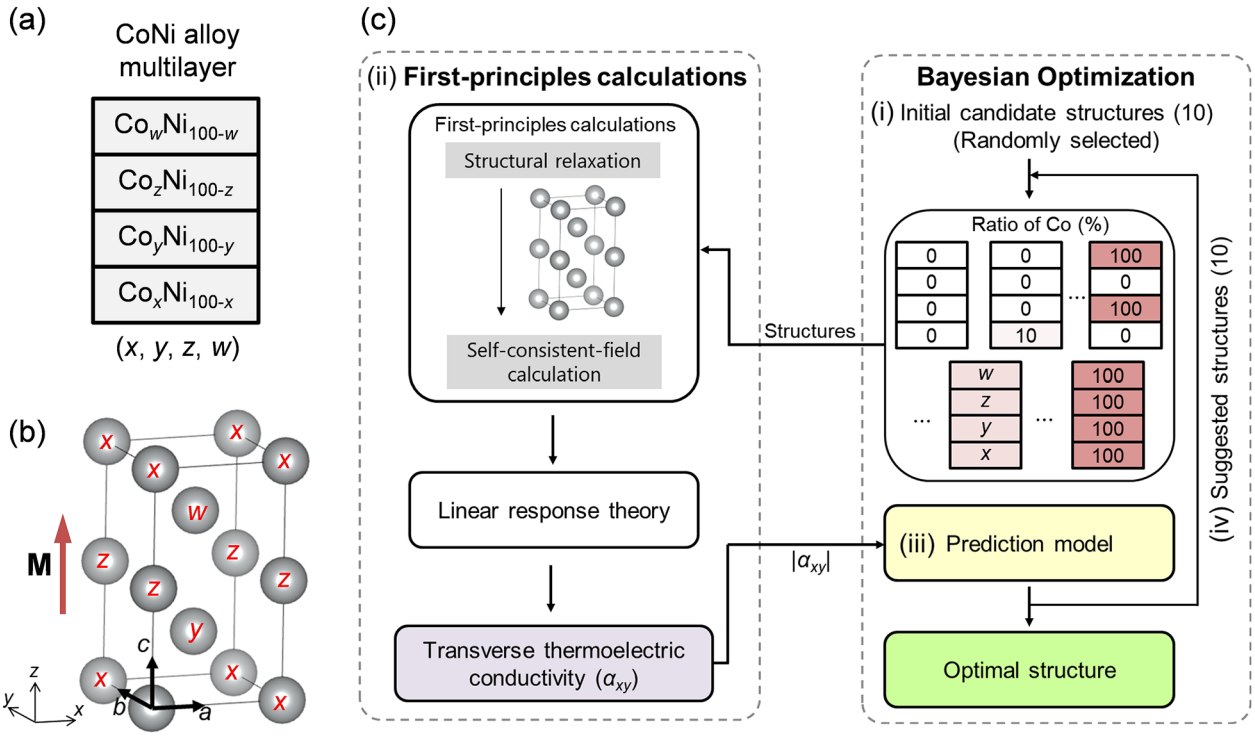

FIG. 1. (a) and (b) A schematic (a) and corresponding crystal structure (b) of the four-layer CoNi homogeneous alloy superlattice. The composition ratio of each layer (*x*, *y*, *z*, *w*) was determined by Bayesian optimization. **M** shows the direction of the magnetization in the first principles calculations. (c) Flowchart of the materials informatics method based on the combination of Bayesian optimization and first-principles calculations for designing the composition ratio of each layer so as to maximize the magnitude of the transverse thermoelectric conductivity $|\alpha_{xy}|$.

conversion performance. In this study, we demonstrate the usability of MI methods in designing ANE materials. Here, we focus on homogeneous alloy multilayers, which particularly increase the number of candidates and are thus yet to be explored, and optimize the compositions of four-layer CoNi homogeneous alloy superlattice systems to increase the transverse thermoelectric performance. The ferromagnetic combination of Co and Ni was adapted for the exploration of a new material category, the convenience of alloy calculations, and the recent improvement in the accuracy of Co/Ni multilayer sample preparation.[52] The composition ratio of each layer was optimized by combining first-principles calculations with Bayesian optimization so as to maximize α_{xy}. The resultant α_{xy} for the CoNi alloy superlattices reached much larger values than the experimentally obtained value. By analyzing the Berry curvature and band dispersion of the obtained optimal structure, we found that a large α_{xy} is attributed to the flat band near the Fermi level due to the optimal multilayer formation. The MI-based method demonstrated here may expand the possibility of ANE enhancement in complex and nonintuitive systems, which have never been explored so far.

II. METHODOLOGY

To obtain α_{xy} of the CoNi alloy superlattice, we performed first-principles calculations based on the density-functional theory (DFT) combined with the linear response theory using the Vienna *ab initio* simulation program (VASP).[53] We constructed the tetragonal superlattice composed of a four-layer CoNi homogeneous alloy superlattice with different compositions as shown in Figs. 1(a) and 1(b), where the Co composition ratio of each layer (x, y, z, w) was optimized via the Bayesian optimization process. For example, if (0, 20, 50, 80) is selected, the alloy multilayer consisting of 0%, 20%, 50%, and 80% Co ratios from bottom to top in Figs. 1(a) and 1(b) is constructed as a calculation target. We adopted the virtual crystal approximation (VCA)[54] to treat alloying effects in the CoNi alloy multilayer. The DFT and VCA have been applied to the calculation of ANE in a previous study.[27,55] In the previous study, ANEs of $Co_3In_xSn_{2-x}S_2$ were calculated using the DFT and VCA, and the dependence of ANE on In concentration was compared with experimental results. As shown in Fig. 4(a) of Ref. 55, the In concentration dependence of ANE by VCA shows a good agreement with the experimental results, suggesting the effectiveness of DFT and VCA in ANE calculations. After constructing the unit cell, we performed self-consistent-field calculations under the periodic boundary condition to obtain the electronic structure using the plane-wave method based on the projector augmented-wave potential,[56,57] including the spin–orbit interaction. The generalized gradient approximation[58] was adopted for the exchange-correlation energy in which the Coulomb interaction U = 3.9 eV and the Hund coupling J = 1.1 eV were taken into account for Ni 3d states.[59] In Ref. 59, the values of U and J for Ni 3d were determined in order to reproduce the experimental α_{xy} of fcc-Ni. A relaxation calculation of the lattice constant and atomic positions was carried out until the atomic force became less than 10^{-2} eV/Å to determine the energetically favored crystal structure of the selected multilayer.[60] After the self-consistent-field calculation, we calculated the anomalous Hall conductivity σ_{xy} derived from the Kubo formula,[61]

$$\sigma_{xy}(\varepsilon) = -\frac{e^2}{\hbar}\int \frac{d^3k}{(2\pi)^3}\Omega^z(\mathbf{k},\varepsilon). \tag{3}$$

$\Omega^z(\mathbf{k},\varepsilon)$ is the Berry curvature, which is given by[62]

$$\Omega^z(\mathbf{k},\varepsilon) = \sum_{m\neq n}\Omega^z_{mn}(\mathbf{k},\varepsilon), \tag{4}$$

$$\Omega^z_{mn}(\mathbf{k},\varepsilon) = \hbar^2[\theta(E_{m,\mathbf{k}},\varepsilon) - \theta(E_{n,\mathbf{k}},\varepsilon)] \times \frac{\mathrm{Im}\langle\psi_{n,\mathbf{k}}|v_x|\psi_{m,\mathbf{k}}\rangle\langle\psi_{m,\mathbf{k}}|v_y|\psi_{n,\mathbf{k}}\rangle}{(E_{n,\mathbf{k}} - E_{m,\mathbf{k}})^2}, \tag{5}$$

where m and n are the band indices, v_x (v_y) is the x (y) component of the velocity operator, $\psi_{n,\mathbf{k}}$ is the eigenstate with the eigenenergy $E_{n,\mathbf{k}}$, and $\theta(E_{n,\mathbf{k}},\varepsilon)$ is the occupation function for the band n and wave vector $\mathbf{k}$ at the energy ε relative to the Fermi energy. In the σ_{xy} calculation, the **M** direction was set to be along the c axis, and the k-point mesh of 64 × 64 × 32 was used for the Brillouin-zone integration, ensuring good convergence for σ_{xy}. The α_{xy} for a given temperature

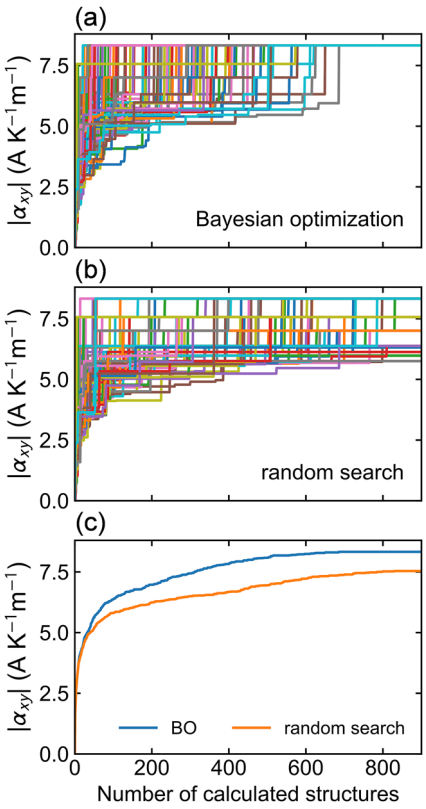

FIG. 2. Performance of the Bayesian optimization for the four-layer CoNi alloy superlattice systems with the candidate pool composed of the composition ratio in 10% intervals. (a) and (b) Dependence of the maximum $|\alpha_{xy}|$ on the number of calculated structures in 100 optimization runs with different initial choices of candidates for the Bayesian optimization (a) and random search (b). Different colors show different initial candidates. (c) Comparison of the averaged maximum $|\alpha_{xy}|$ trends in 100 optimization runs.

T was calculated by substituting the obtained σ_{xy} into the following expression derived from the Boltzmann transport theory:

$$\alpha_{xy} = -\frac{1}{eT}\int d\varepsilon\left(-\frac{\partial f}{\partial \varepsilon}\right)(\varepsilon-\mu)\sigma_{xy}(\varepsilon), \tag{6}$$

where $f = 1/[\exp((\varepsilon-\mu)/k_B T) + 1]$ is the Fermi distribution function with μ being the chemical potential. The absolute value of α_{xy} for $T = 300$ K at the Fermi energy, $\mu = 0$ eV, was adopted as the evaluator for the Bayesian optimization.

To find the optimal structure with the highest α_{xy} efficiently, the Bayesian optimization was combined with the above-mentioned first-principles calculation, which was carried out using the open-source Bayesian optimization library COMBO.[63] Hereafter, we use the magnitude of α_{xy}, $|\alpha_{xy}|$, as the target property in the optimization to properly evaluate negative α_{xy}. We prepared the candidate pool by regarding (x, y, z, w) as the descriptor; if we set the composition ratio in 10% intervals, 11^4 candidate structures can be obtained in the four-layer CoNi alloy superlattice system unless we consider equivalent structures. After the preparation of the candidate pool, the following procedure was then conducted as shown in Fig. 1(c): (i) randomly selecting ten initial structures from the prepared pool; (ii) calculating the corresponding $|\alpha_{xy}|$ as the evaluator; (iii) training the prediction model for $|\alpha_{xy}|$ with the dataset of the descriptors and evaluators calculated so far; and (iv) selecting the next ten candidates according to the probability of being optimal. By repeating the processes (ii)–(iv), the optimal structure with the highest $|\alpha_{xy}|$ can be efficiently identified. As the prediction model in (iii), we employed the Bayesian linear regression model following the relation:

$$|\alpha_{xy}| = \mathbf{w}^{\mathrm{T}}\phi(\mathbf{x}) + \varsigma, \tag{7}$$

where $\mathbf{x} = (x, y, z, w)^{\mathrm{T}}$ is the four-dimensional vector corresponding to the composition ratios of a candidate structure, ϕ is the random feature map including l basis functions, $\mathbf{w}$ is the l-dimensional weight vector, and ς is the noise subject to a normal distribution with a mean of 0 and variance σ. The random feature map is defined so that the inner product $\phi(\mathbf{x})\ \phi(\mathbf{x}')$ approximates the Gaussian kernel of width η, i.e., $\exp(-||\mathbf{x} - \mathbf{x}'||^2/2\eta^2)$.[64] The hyperparameters σ and η, which determine the performance of the optimization, were automatically initialized[65] and tuned[66] between processes (iii)

(a) 10 % intervals

type	x	y	z	w	$\lvert\alpha_{xy}\rvert$ (A K^{-1} m^{-1})
1	10	80	40	80	8.3
2	20	30	40	50	7.6
1	10	80	50	90	7.0
1	10	80	40	90	6.4
1	0	90	40	90	6.3
2	0	20	30	60	6.1
0	50	60	50	100	6.0
1	0	100	50	100	5.9
0	10	20	90	40	5.8
1	0	80	50	80	5.7
0	0	0	0	80	5.7
1	10	90	50	90	5.7
0	0	70	20	90	5.6
2	20	50	20	60	5.6
2	10	50	30	60	5.6
1	0	90	60	90	5.5
1	0	80	60	90	5.4
1	0	90	50	90	5.3
2	30	30	40	40	5.3
2	20	30	50	40	5.3

(b) 1 % intervals in (0-10, 80-90, 40-50, 80-90)

x	y	z	w	$\lvert\alpha_{xy}\rvert$ (A K^{-1} m^{-1})
3	85	40	80	10.1
2	85	40	81	9.6
4	82	40	81	9.5
4	84	41	81	9.2
2	80	41	83	8.9
4	82	41	81	8.8
0	85	42	80	8.7
4	81	41	81	8.5
4	81	42	82	8.3
3	81	41	83	8.2
3	81	42	80	8.2
4	82	42	80	8.2
4	84	41	80	8.2
4	80	42	83	8.1
4	82	40	80	8.1
2	85	41	80	8.0
5	83	41	82	7.9
4	83	42	81	7.9
10	80	41	81	7.8
9	84	48	83	7.6

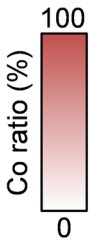

FIG. 3. Schematics and $|\alpha_{xy}|$ of the top 20 four-layer CoNi alloy superlattice structures in the Bayesian optimization using the candidate pools with the composition ratio in 10% intervals (a) and in 1% intervals in (0-10, 80-90, 40-50, 80-90) (b). The structural types are also shown for (a). The colors of the schematic correspond to the Co ratio.

and (iv). More details on the procedure of COMBO can be found elsewhere.[41,46,63]

III. RESULTS AND DISCUSSIONS

A. Bayesian optimization

To test the performance of the Bayesian optimization, 100 rounds of the optimization were conducted with different choices of 10 initial candidates using a candidate pool consisting of structures with composition ratios in 10% intervals. A random search using the same initial candidates as the Bayesian optimization was also performed for comparison. As shown in Figs. 2(a) and 2(b), the maximum $|\alpha_{xy}|$ comes to convergence within the calculations of 650 structures for the Bayesian optimization, while more than half of the random searches have not yet reached such convergence at that number of the calculated structures. Figure 2(c) shows the comparison of averaged maximum $|\alpha_{xy}|$ trends, clearly indicating the superiority of the Bayesian optimization. In addition, the average number of calculations required to find the optimal structure is about 256, which is only 11.6% of the total number of candidates (=2211), indicating the effectiveness of the optimization (note that the number 2211 was obtained by counting nonequivalent structures from 11^4 candidates). The $|\alpha_{xy}|$ calculations for all candidates were also performed to check the accuracy of the optimization, and the highest one was confirmed to be the same as that obtained by the Bayesian optimization. As shown in Fig. 3(a), many of the top 20 structures have a similar trend of the descriptor, and compositional trends with large $|\alpha_{xy}|$ can be categorized into two types: type 1 (0–20, 80–100, 40–60, 80–100) and type 2 (0–30, 20–50, 30–50, 40–60), although there are some exceptional structures (defined as type 0). In particular, type 1 accounts for half of the top 20 structures, four of which are large $|\alpha_{xy}|$ enough to rank in the top five. This correlation between the descriptors (x, y, z, w) and the evaluator $|\alpha_{xy}|$ may lead to the effectiveness of the Bayesian optimization for the CoNi alloy superlattice system used here.

For further enhancement of $|\alpha_{xy}|$, we carried out the Bayesian optimization using the candidates composed of structures with finer composition ratios. To conduct the optimization efficiently, the candidates were limited based on the results of Fig. 3(a) obtained in the above-mentioned optimization. Since type 1 structures exhibit large $|\alpha_{xy}|$ as mentioned in the last paragraph, we selected the candidates with composition ratios of (0–10, 80–90, 40–50, and 80–90) with 1% intervals, which correspond to all structures with intermediate composition ratios in 1% increments in the top-five ranked structures among the type 1. Figure 3(b) shows the optimization result with the calculation of 100 structures, which is only 0.68% of all candidates (=11^4, where there is no equivalent structure). Compared to Fig. 3(a) (10% intervals), the largest $|\alpha_{xy}|$ further increased in the finer candidates, and its structure was found to be (3, 85, 40, 80), which is impossible to predict intuitively (note that this structure is not necessarily the true global optimal structure because the optimal structure that can be correctly identified by the Bayesian optimization is limited to the case of $|\alpha_{xy}|$ having a relatively monotonic dependence on the composition ratio). Through two-step optimization with rough and fine candidate pools, we identified the nonintuitive structure whose $|\alpha_{xy}|$ is a large value of 10.1 A K^{-1} m^{-1}. Despite only using Co ($|\alpha_{xy}|$ = 1.4 A K^{-1} m^{-1}) and Ni ($|\alpha_{xy}|$ = 0.9 A K^{-1} m^{-1}), the one-order-of-magnitude increase in $|\alpha_{xy}|$ was achieved by layer-by-layer stacking of the CoNi homogeneous alloy films with different compositions [note that $|\alpha_{xy}|$ of Co and Ni were obtained as those of the structures of (100, 100, 100, 100) and (0, 0, 0, 0) in the descriptor, respectively].

B. Analysis of optimal structure

We now discuss the origin of the large $|\alpha_{xy}|$ in the optimal structure. The blue curve in Fig. 4(c) shows α_{xy} of the optimized (x, y, z, w) superlattice as a function of the chemical potential μ, where μ = 0 eV corresponds to the Fermi energy. To confirm the effectiveness of multilayer formation, we compared the transport properties of the optimal structure with those of the simple structure, which is a non-multilayered CoNi homogeneous alloy with the same total composition ratio as the optimal structure [schematically depicted in Fig. 4(a)]. In Figs. 4(b) and 4(c), we compare the μ dependence of σ_{xy} and α_{xy} for the optimal and simple structures. As shown in Fig. 4(b), σ_{xy} changes rapidly near the Fermi energy for the optimal structure, while the μ dependence is relatively smooth for the simple

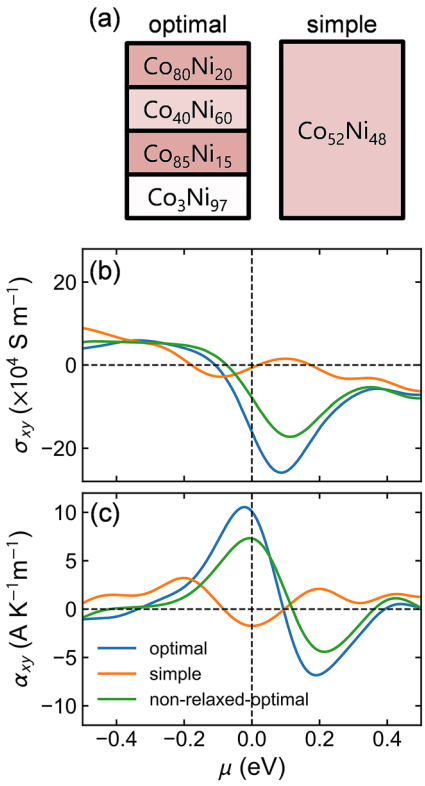

FIG. 4. (a) Schematics of the optimal four-layer CoNi alloy superlattice and simple non-multilayered structures. (b) and (c) Chemical potential μ dependence of the anomalous Hall conductivity σ_{xy} (b) and α_{xy} (c) for the optimal, simple, and non-relaxed-optimal structures. The last one means the structure with the optimal composition ratio of each layer whose lattice constant and atomic positions are the same as the simple structure.

structure. Following the Mott relation derived from the Sommerfeld expansion, Eq. (6) becomes[67]

$$\alpha_{xy} = -\frac{\pi^2}{3}\frac{k_B^2 T}{e}\left(\frac{\partial \sigma_{xy}}{\partial \varepsilon}\right)_{\varepsilon=\mu}, \tag{8}$$

where k_B is the Boltzmann constant, showing that the absolute value of α_{xy} is proportional to the energy derivative of σ_x. Therefore, the optimal structure with a large $\partial\sigma_{xy}/\partial\varepsilon$ exhibits a larger α_{xy} at Fermi energy compared to the simple structure. Furthermore, in order to clarify the lattice distortion effect on α_{xy} of the optimal structure, we also calculated the transport properties of a non-relaxed optimal structure, which is the structure with the optimal composition ratio whose lattice constant and atomic positions are the same as the simple structure. As can be seen in Fig. 4(b), the non-relaxed optimal structure shows a similar σ_{xy} trend to the optimal structure, indicating that the large α_{xy} in the optimized superlattice is mainly due to the multilayer formation and the effect of the lattice distortion is relatively small. Furthermore, the local concentration fluctuations in in-plane (xy) directions will lead to the reduction of AHE and

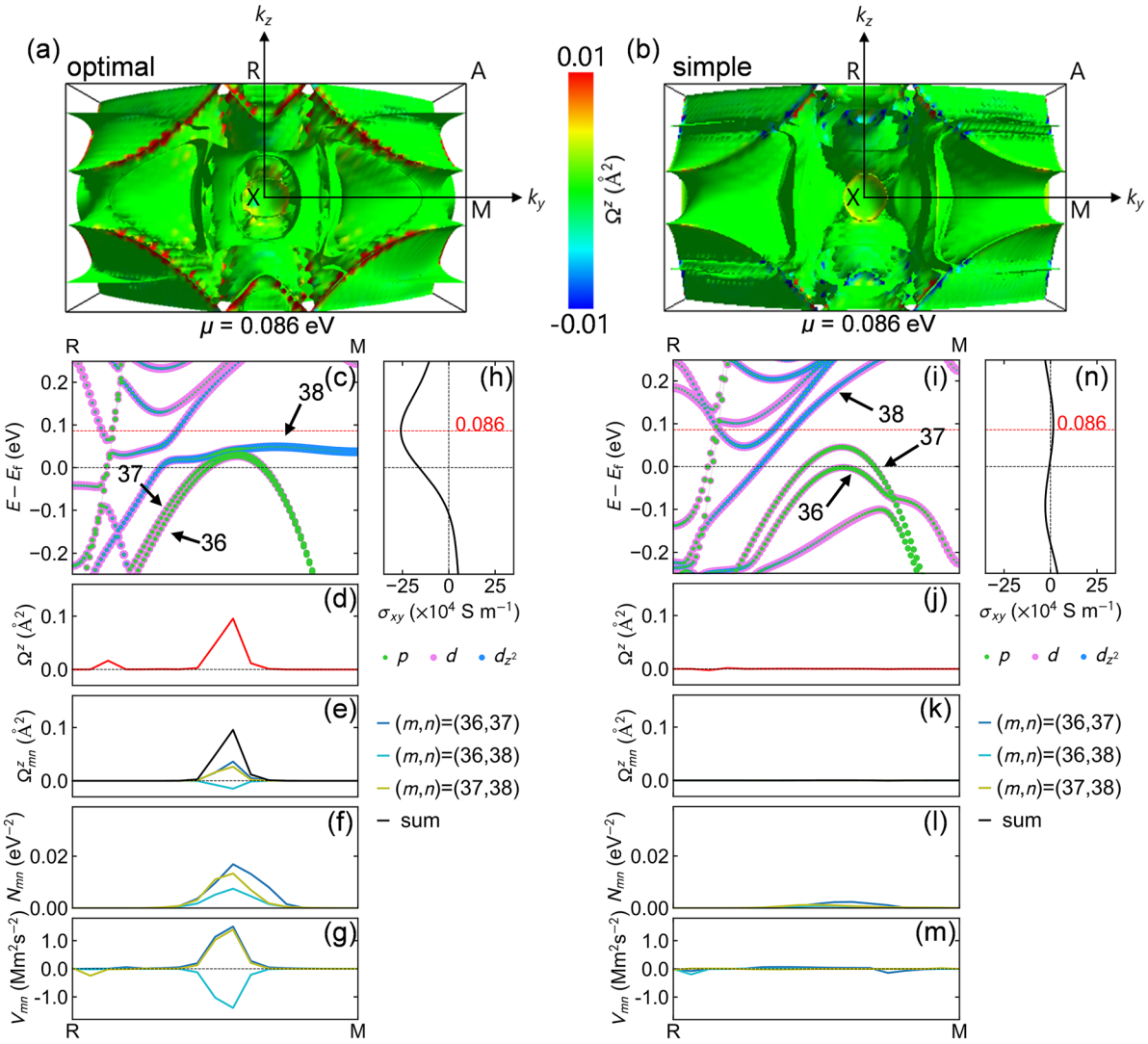

FIG. 5. (a) and (b) Color maps of the Berry curvatures $\Omega^z(\mathbf{k},\varepsilon)$ at μ = 0.086 eV for the optimal (a) and simple (b) structures plotted on the iso-energy surface in the three-dimensional first Brillouin zone, which are visualized with FermiSurfer.[71] (c)–(g) k-points dependence of physical properties related to the band structure and Berry curvature along the R-M line for the optimal structures: (c) band structures with the weights of the p (green), d (pink), and d_{z^2} (blue) orbitals being represented by the size of the symbol, (d) Berry curvatures $\Omega^z(\mathbf{k},\varepsilon)$ in Eq. (4), (e) inter-band decomposed Berry curvatures $\Omega_{mn}{}^z(\mathbf{k},\varepsilon)$ in Eq. (5) among the 36th, 37th, and 38th bands, (f) the denominator part of $\Omega_{mn}{}^z(\mathbf{k},\varepsilon)$ with occupation function denoted as $N_{mn}(\mathbf{k},\varepsilon)$ in Eq. (9), and (g) the numerator part of $\Omega_{mn}{}^z(\mathbf{k},\varepsilon)$ without occupation function denoted as $V_{mn}(\mathbf{k})$ in Eq. (10). In (e), the total contribution among these bands is also plotted as a black line. (h) μ dependence of σ_{xy} on the optimal structure, as also shown in Fig. 4(b). (i)–(n) The same physical properties as (c)–(h) for the simple structure, respectively. Multimedia view: https://doi.org/10.1063/5.0140332.1

ANE because the randomness along the in-plane direction increases the resistivity and decreases the conductivity in xy directions. This means that the fabrication of homogeneous CoNi alloys along in-plane directions will be required to obtain the large ANE in the multilayered system.

Next, we contemplated the Berry curvature to clarify the origin of the large σ_{xy} slope at the Fermi energy. To identify the locations of k-points that contribute to the entire σ_{xy} change in Eq. (3), we mapped $\Omega^z(\mathbf{k},\varepsilon)$ onto the iso-energy surface at $\mu = 0.086$ eV, where σ_{xy} shows the largest peak. As shown in Figs. 5(a) and 5(b), the Berry curvatures of the optimal structure exhibit positive peaks on the k_y–k_z plane at $k_x = 0.5$, especially on the R-M line, while those of the simple structure have few peaks on the same scale compared to the optimal structure, resulting in relatively small $\partial\sigma_{xy}/\partial\varepsilon$ and α_{xy}. In order to shed light on the mechanism of the $\Omega^z(\mathbf{k},\varepsilon)$ difference between the optimal and simple structures, we calculated the band dispersion along the R-M line, which has many $\Omega^z(\mathbf{k},\varepsilon)$ peaks in the optimal structure. The band dispersions of the optimal and simple structures are presented in Figs. 5(c) and 5(i). Compared to the simple structure, the flat 38th band emerges in the band dispersion of the optimal structure, which is located close to the 36th and 37th bands around the middle of the R-M line. Correspondingly, as shown in Fig. 5(d), $\Omega^z(\mathbf{k},\varepsilon)$ of the optimal structure at $\mu = 0.086$ eV has large peaks at the band proximity points among the 36th–38th bands. This relationship can be interpreted as follows: In Eq. (5), the occupation function $\theta(E_{n,\mathbf{k}},\varepsilon)$ changes only near the chemical potential $\mu = 0.086$ eV from 1 to 0. Additionally, $\Omega_{mn}{}^z(\mathbf{k},\varepsilon)$ has a large contribution to the entire $\Omega^z(\mathbf{k},\varepsilon)$ only when the energy gap in the denominator takes a small value. Therefore, large $\Omega^z(\mathbf{k},\varepsilon)$ peaks are attributed to the band proximity points among the 36th–38th bands, which are located around $\mu = 0.086$ eV (red dashed line). In fact, by calculating each contribution of $\Omega_{mn}{}^z(\mathbf{k},\varepsilon)$ of the optimal structure at the largest peak k-point on the R-M line from $\mu = -0.25$ to 0.25 eV, we confirmed that only contributions among the 36th–38th bands have the largest magnitude, while the largest contribution in the simple structure was at most two orders of magnitude smaller than that in the optimal structure.

To gain further insights into the contributions of the 36th–38th bands, we considered the effects of d-p orbital hybridizations in the Berry curvature. The weights of p, d, and d_{z^2} orbitals[68] are respectively represented as the sizes of green, pink, and blue markers in the band dispersion of Figs. 5(c) and 5(i). In the optimal structure, the orbital weight of d_{z^2} is dominant in the 38th flat band, while the 36th and 37th bands have not only d-orbital but also p-orbital contributions around the $\Omega^z(\mathbf{k},\varepsilon)$ peak point. This orbital weight distribution is also important for understanding the Berry curvature. Since the matrix element of the velocity operator between arbitrary two states divided by the difference in the eigenvalues corresponds to the matrix element of the dipole operator, only transitions between states of different parity are permitted due to the selection rule of the dipole transitions.[69] In our case, d-p transitions occur around the band proximity points. Hence, matrix elements of the velocity operator between the 36th–37th, 36th–38th, and 37th–38th bands can contribute to the entire $\Omega^z(\mathbf{k},\varepsilon)$, resulting in the enhancement of α_{xy} in the optimal structure. The proximity of these bands is due to the emergence of the additional 38th flat band that does not exist in the simple structure, indicating the importance of multilayer formation.

To confirm the effect of d-p orbital transitions quantitatively, we calculated $\Omega_{mn}{}^z(\mathbf{k},\varepsilon)$ [Eq. (5)], $N_{mn}(\mathbf{k},\varepsilon)$, and $V_{mn}(\mathbf{k})$, where

$$N_{mn}(\mathbf{k},\varepsilon) = [\theta(E_{m,\mathbf{k}},\varepsilon) - \theta(E_{n,\mathbf{k}},\varepsilon)]\frac{1}{(E_{n,\mathbf{k}} - E_{m,\mathbf{k}})^2}, \tag{9}$$

$$V_{mn}(\mathbf{k}) = \mathrm{Im}\langle\psi_{n,\mathbf{k}}|v_x|\psi_{m,\mathbf{k}}\rangle\langle\psi_{m,\mathbf{k}}|v_y|\psi_{n,\mathbf{k}}\rangle. \tag{10}$$

$N_{mn}(\mathbf{k},\varepsilon)$ corresponding to the denominator of Eq. (5) with occupation functions represents the inverse of the eigenenergy gap between mth and nth eigenstates, while $V_{mn}(\mathbf{k})$, the numerator of Eq. (5) without occupation functions, stands for the matrix elements of the velocity operator between mth and nth eigenstates. In Fig. 5(e), the inter-band decomposed Berry curvature $\Omega_{mn}{}^z(\mathbf{k})$ with $(m, n) = (36, 37)$, $(36, 38)$, and $(37, 38)$, and their total contributions are presented at $\mu = 0.086$ eV. They show that $\Omega_{mn}{}^z(\mathbf{k})$ of the 36th–38th bands (black line) exhibits an almost similar trend to the entire $\Omega^z(\mathbf{k})$ [Fig. 5(d)] around the largest peak k-point, confirming that the entire $\Omega^z(\mathbf{k},\varepsilon)$ is ascribed to the contributions among the 36th–38th bands [multimedia view]. As shown in Figs. 5(f) and 5(g), although both $N_{mn}(\mathbf{k},\varepsilon)$ and $V_{mn}(\mathbf{k})$ have finite values in the peak k-points, a wider peak is observed for $N_{mn}(\mathbf{k},\varepsilon)$ derived from the 36th–37th transition.[70] In the 36th and 37th bands, the weight of the d-orbital (pink marker) decreases with approaching the M point, which leads to the reduction of $V_{mn}(\mathbf{k})$. On the other hand, the 36th and 37th bands still have a small energy gap at these k-points, leading to a small $\Omega_{mn}{}^z(\mathbf{k},\varepsilon)$ ($\sim N_{mn} \times V_{mn}$) despite a large $N_{mn}(\mathbf{k},\varepsilon)$. Therefore, we consider that not only the small eigenenergy gap but also finite matrix elements are essential for the α_{xy} enhancement in the CoNi alloy multilayer system.

IV. CONCLUSIONS

In conclusion, we demonstrated the enhancement of transverse thermoelectric performance by designing the superlattices of the homogeneous alloy films with different compositions consisting only of typical ferromagnets Co and Ni with the aid of the machine learning method. We identified the four-layer CoNi alloy superlattice, which has a large $|\alpha_{xy}|$ of ~10 A K^{-1} m^{-1} by combining the Bayesian optimization and first-principles calculations. The composition ratio of each layer was successfully optimized by performing a two-step Bayesian optimization with the rough and fine candidate pools, where only a few percent of the total candidates were needed to find the optimal structure, leading to a significant reduction in computational cost. From the comparison of the optimal superlattice structure with a simple non-multilayered CoNi alloy, we found that the optimized superlattice with the adjusted composition ratio of each layer enhanced the magnitude of the energy derivative of σ_{xy} at the Fermi energy, resulting in a large α_{xy}. Furthermore, the Berry curvature and band dispersion analyses identified that this large $\partial\sigma_{xy}/\partial\varepsilon$ at the Fermi energy is attributed to the emergence of the flat band brought about by the multilayer formation in the optimal structure. The optimized superlattice has a flat band consisting of d-orbitals near the Fermi energy along the R-M line, where the other two bands dominated by p- and d-orbitals are also located. Consequently, the proximity of these flat bands and other bands enables the d-p dipole transitions near the Fermi level, leading to

large α_{xy} in the four-layer CoNi alloy superlattices. The method of combining materials informatics and simulations used in this study will be applicable to various systems or materials for the further enhancement of α_{xy} if they can be represented by descriptors. The fabrication of homogeneous mono-layered CoNi alloys with multiple layers may be difficult with current experimental techniques. However, we found many candidates showing a large ANE using Bayesian optimization. Since the technology of thin film fabrication is advancing day by day, as reported in Ref. 52, we believe that, in the near future, it will be possible to fabricate homogeneous alloy thin films. Furthermore, our study suggests the effectiveness of Bayesian optimization to find materials with a larger ANE and the importance of the localization of the wavefunctions by multilayering to enhance the Berry curvature and the ANE coefficient, which will be suggestive for future experiments on ANE. Therefore, the method demonstrated here may contribute to finding new principles and materials for the transverse thermoelectric conversion and improving its performance.

SUPPLEMENTARY MATERIAL

The data and code supporting the findings of this study are provided in the supplementary material.

ACKNOWLEDGMENTS

The authors acknowledge J. Shiomi, R. Modak, and S. Biswas for their valuable discussions. This work was partly supported by Grants-in-Aid for Scientific Research (Grant No. JP16H06332) from JSPS, CREST "Creation of Innovative Core Technologies for Nano-enabled Thermal Management" (Grant No. JPMJCR17I1), and ERATO "Magnetic Thermal Management Materials" (Grant No. JPMJER2201), both from JST, Japan.

AUTHOR DECLARATIONS

Conflict of Interest

The authors have no conflicts to disclose.

Author Contributions

Naoki Chiba: Data curation (lead); Formal analysis (lead); Investigation (lead); Visualization (lead); Writing – original draft (lead). **Keisuke Masuda**: Investigation (supporting); Methodology (equal); Writing – review & editing (supporting). **Ken-ichi Uchida**: Funding acquisition (lead); Project administration (lead); Supervision (equal); Writing – review & editing (supporting). **Yoshio Miura**: Conceptualization (lead); Methodology (supporting); Resources (lead); Supervision (equal); Writing – review & editing (equal).

DATA AVAILABILITY

The data that support the findings of this study are available within the article and its supplementary material.

REFERENCES

[1] M. Hatami, G. E. W. Bauer, Q. Zhang, and P. J. Kelly, Phys. Rev. Lett. **99**, 066603 (2007).
[2] G. E. W. Bauer, E. Saitoh, and B. J. Van Wees, Nat. Mater. **11**, 391 (2012).
[3] K. Uchida, Proc. Jpn. Acad., Ser. B **97**, 69 (2021).
[4] K. Uchida, S. Takahashi, K. Harii, J. Ieda, W. Koshibae, K. Ando, S. Maekawa, and E. Saitoh, Nature **455**, 778 (2008).
[5] K. Uchida, H. Adachi, T. Ota, H. Nakayama, S. Maekawa, and E. Saitoh, Appl. Phys. Lett. **97**, 172505 (2010).
[6] K. Uchida, J. Xiao, H. Adachi, J. Ohe, S. Takahashi, J. Ieda, T. Ota, Y. Kajiwara, H. Umezawa, H. Kawai, G. E. W. Bauer, S. Maekawa, and E. Saitoh, Nat. Mater. **9**, 894 (2010).
[7] C. M. Jaworski, J. Yang, S. MacK, D. D. Awschalom, J. P. Heremans, and R. C. Myers, Nat. Mater. **9**, 898 (2010).
[8] J. P. Jan, in *Solid State Physics*, edited by F. Seitz and D. Turnbull (Academic, New York, 1957), Vol. 5, p. 1.
[9] J.-E. Wegrowe, Q. A. Nguyen, M. Al-Barki, J.-F. Dayen, T. L. Wade, and H.-J. Drouhin, Phys. Rev. B **73**, 134422 (2006).
[10] M. Walter, J. Walowski, V. Zbarsky, M. Münzenberg, M. Schäfers, D. Ebke, G. Reiss, A. Thomas, P. Peretzki, M. Seibt, J. S. Moodera, M. Czerner, M. Bachmann, and C. Heiliger, Nat. Mater. **10**, 742 (2011).
[11] K. S. Das, F. K. Dejene, B. J. Van Wees, and I. J. Vera-Marun, Phys. Rev. B **94**, 180403 (2016).
[12] K. Uchida, S. Daimon, R. Iguchi, and E. Saitoh, Nature **558**, 95 (2018).
[13] K. Masuda, K. Uchida, R. Iguchi, and Y. Miura, Phys. Rev. B **99**, 104406 (2019).
[14] T. Miyasato, N. Abe, T. Fujii, A. Asamitsu, S. Onoda, Y. Onose, N. Nagaosa, and Y. Tokura, Phys. Rev. Lett. **99**, 086602 (2007).
[15] Y. Pu, D. Chiba, F. Matsukura, H. Ohno, and J. Shi, Phys. Rev. Lett. **101**, 117208 (2008).
[16] K. Hasegawa, M. Mizuguchi, Y. Sakuraba, T. Kamada, T. Kojima, T. Kubota, S. Mizukami, T. Miyazaki, and K. Takanashi, Appl. Phys. Lett. **106**, 252405 (2015).
[17] K. Uchida, T. Kikkawa, T. Seki, T. Oyake, J. Shiomi, Z. Qiu, K. Takanashi, and E. Saitoh, Phys. Rev. B **92**, 094414 (2015).
[18] C. Fang, C. H. Wan, Z. H. Yuan, L. Huang, X. Zhang, H. Wu, Q. T. Zhang, and X. F. Han, Phys. Rev. B **93**, 054420 (2016).
[19] M. Ikhlas, T. Tomita, T. Koretsune, M.-T. Suzuki, D. Nishio-Hamane, R. Arita, Y. Otani, and S. Nakatsuji, Nat. Phys. **13**, 1085 (2017).
[20] H. Reichlova, R. Schlitz, S. Beckert, P. Swekis, A. Markou, Y.-C. Chen, D. Kriegner, S. Fabretti, G. Hyeon Park, A. Niemann, S. Sudheendra, A. Thomas, K. Nielsch, C. Felser, and S. T. B. Goennenwein, Appl. Phys. Lett. **113**, 212405 (2018).
[21] A. Sakai, Y. P. Mizuta, A. A. Nugroho, R. Sihombing, T. Koretsune, M.-T. Suzuki, N. Takemori, R. Ishii, D. Nishio-Hamane, R. Arita, P. Goswami, and S. Nakatsuji, Nat. Phys. **14**, 1119 (2018).
[22] H. Nakayama, K. Masuda, J. Wang, A. Miura, K. Uchida, M. Murata, and Y. Sakuraba, Phys. Rev. Mater. **3**, 114412 (2019).
[23] A. Miura, H. Sepehri-Amin, K. Masuda, H. Tsuchiura, Y. Miura, R. Iguchi, Y. Sakuraba, J. Shiomi, K. Hono, and K. Uchida, Appl. Phys. Lett. **115**, 222403 (2019).
[24] X. Zhou, J. P. Hanke, W. Feng, S. Blügel, Y. Mokrousov, and Y. Yao, Phys. Rev. Mater. **4**, 024408 (2020).
[25] Y. Sakuraba, K. Hyodo, A. Sakuma, and S. Mitani, Phys. Rev. B **101**, 134407 (2020).
[26] A. Sakai, S. Minami, T. Koretsune, T. Chen, T. Higo, Y. Wang, T. Nomoto, M. Hirayama, S. Miwa, D. Nishio-Hamane, F. Ishii, R. Arita, and S. Nakatsuji, Nature **581**, 53 (2020).
[27] A. Miura, K. Masuda, T. Hirai, R. Iguchi, T. Seki, Y. Miura, H. Tsuchiura, K. Takanashi, and K. Uchida, Appl. Phys. Lett. **117**, 082408 (2020).
[28] T. Seki, Y. Sakuraba, K. Masuda, A. Miura, M. Tsujikawa, K. Uchida, T. Kubota, Y. Miura, M. Shirai, and K. Takanashi, Phys. Rev. B **103**, L020402 (2021).
[29] S. Isogami, K. Masuda, Y. Miura, N. Rajamanickam, and Y. Sakuraba, Appl. Phys. Lett. **118**, 092407 (2021).
[30] T. Asaba, V. Ivanov, S. M. Thomas, S. Y. Savrasov, J. D. Thompson, E. D. Bauer, and F. Ronning, Sci. Adv. **7**, eabf1467 (2021).

[31] Y. Pan, C. Le, B. He, S. J. Watzman, M. Yao, J. Gooth, J. P. Heremans, Y. Sun, and C. Felser, Nat. Mater. **21**, 203 (2022).
[32] H. K. Singh, I. Samathrakis, C. Shen, and H. Zhang, Phys. Rev. Mater. **6**, 045402 (2022).
[33] K. Uchida, W. Zhou, and Y. Sakuraba, Appl. Phys. Lett. **118**, 140504 (2021).
[34] K. Uchida and J. P. Heremans, Joule **6**, 2240 (2022).
[35] M. V. Berry, Proc. R. Soc. Lond. A **392**, 45 (1984).
[36] C. Klewe, T. Kuschel, J.-M. Schmalhorst, F. Bertram, O. Kuschel, J. Wollschläger, J. Strempfer, M. Meinert, and G. Reiss, Phys. Rev. B **93**, 214440 (2016).
[37] T. Kikkawa, M. Suzuki, R. Ramos, M. H. Aguirre, J. Okabayashi, K. Uchida, I. Lucas, A. Anadón, D. Kikuchi, P. A. Algarabel, L. Morellón, M. R. Ibarra, and E. Saitoh, J. Appl. Phys. **126**, 143903 (2019).
[38] K. Meng, J. Xiao, Y. Wu, J. Miao, X. Xu, J. Zhao, and Y. Jiang, Sci. Rep. **6**, 020522 (2016).
[39] Z. B. Guo, W. B. Mi, R. O. Aboljadayel, B. Zhang, Q. Zhang, P. G. Barba, A. Manchon, and X. X. Zhang, Phys. Rev. B **86**, 104433 (2012).
[40] K. Rajan, Annu. Rev. Mater. Res. **45**, 153 (2015).
[41] S. Ju and J. Shiomi, Nanoscale Microscale Thermophys. Eng. **23**, 157 (2019).
[42] S. Ju, T. Shiga, L. Feng, Z. Hou, K. Tsuda, and J. Shiomi, Phys. Rev. X **7**, 021024 (2017).
[43] T. M. Dieb, S. Ju, K. Yoshizoe, Z. Hou, J. Shiomi, and K. Tsuda, Sci. Technol. Adv. Mater. **18**, 498 (2017).
[44] T. Zhan, L. Fang, and Y. Xu, Sci. Rep. **7**, 7109 (2017).
[45] T. Yamashita, N. Sato, H. Kino, T. Miyake, K. Tsuda, and T. Oguchi, Phys. Rev. Mater. **2**, 013803 (2018).
[46] M. Yamawaki, M. Ohnishi, S. Ju, and J. Shiomi, Sci. Adv. **4**, eaar4192 (2018).
[47] A. Sakurai, K. Yada, T. Simomura, S. Ju, M. Kashiwagi, H. Okada, T. Nagao, K. Tsuda, and J. Shiomi, ACS Cent. Sci. **5**, 319 (2019).
[48] Z. Hou, Y. Takagiwa, Y. Shinohara, Y. Xu, and K. Tsuda, ACS Appl. Mater. Interfaces **11**, 11545 (2019).
[49] Y.-J. Wu, L. Fang, and Y. Xu, npj Comput. Mater. **5**, 56 (2019).
[50] S. Ju, Y. Miura, K. Yamamoto, K. Masuda, K. Uchida, and J. Shiomi, Phys. Rev. Res. **2**, 023187 (2020).
[51] R. Hu, S. Iwamoto, L. Feng, S. Ju, S. Hu, M. Ohnishi, N. Nagai, K. Hirakawa, and J. Shiomi, Phys. Rev. X **10**, 021050 (2020).
[52] T. Seki, J. Shimada, S. Iihama, M. Tsujikawa, T. Koganezawa, A. Shioda, T. Tashiro, W. Zhou, S. Mizukami, M. Shirai, and K. Takanashi, J. Phys. Soc. Jpn. **86**, 074071 (2017).
[53] G. Kresse and J. Furthmüller, Phys. Rev. B **54**, 11169 (1996).
[54] L. Bellaiche and D. Vanderbilt, Phys. Rev. B **61**, 7877 (2000).
[55] Y. Yanagi, J. Ikeda, K. Fujiwara, K. Nomura, A. Tsukazaki, and M.-T. Suzuki, Phys. Rev. B **103**, 205112 (2021).
[56] P. E. Blöchl, Phys. Rev. B **50**, 17953 (1994).
[57] D. Joubert, Phys. Rev. B **59**, 1758 (1999).
[58] J. P. Perdew, K. Burke, and M. Ernzerhof, Phys. Rev. Lett. **77**, 3865 (1996).
[59] J. Weischenberg, F. Freimuth, S. Blügel, and Y. Mokrousov, Phys. Rev. B **87**, 060406 (2013).
[60] W. H. Press, B. P. Flannery, S. A. Teukolsky, and W. T. Vetterling, in *Numerical Recipes: The Art of Scientific Computing* (Cambridge University Press, New York, 1987), p. 87.
[61] Y. Yao, L. Kleinman, A. H. MacDonald, J. Sinova, T. Jungwirth, D. sheng Wang, E. Wang, and Q. Niu, Phys. Rev. Lett. **92**, 037204 (2004).
[62] Y. Miura and K. Masuda, Phys. Rev. Mater. **5**, L101402 (2021).
[63] T. Ueno, T. D. Rhone, Z. Hou, T. Mizoguchi, and K. Tsuda, Mater. Discov. **4**, 18 (2016).
[64] A. Rahimi and B. Recht, in *Proceedings of the 20th International Conference on Neural Information Processing Systems* (Curran Associates, Inc., Vancouver, BC, 2007), p. 1177.
[65] Z. Yang, A. J. Smola, L. Song, and A. G. Wilson, in Proceedings of the Eighteenth International Conference on Artificial Intelligence and Statistics, AISTATS 2015, San Diego, CA, 9-12 May 2015 [JMLR Proc. **38**, 1098 (2015)].
[66] D. P. Kingma and J. L. Ba, "Adam: A method for stochastic optimization," arXiv:1412.6980 (2015).
[67] N. F. Mott and H. Jones, in *The Theory of the Properties of Metals and Alloys* (Clarendon, Oxford, 1936), p. 308.
[68] p (d) represents the total contribution of all three (five) kinds of p (d) orbitals. d_{Z^2} is the abbreviation of $d_{3z^2-r^2}$ orbital.
[69] A. M. Pradipto, T. Akiyama, T. Ito, and K. Nakamura, Phys. Rev. B **97**, 024401 (2018).
[70] Other $N_{mn}(\mathbf{k},\varepsilon)$ peaks are also observed in the supplementary video at different μ.
[71] M. Kawamura, Comput. Phys. Commun. **239**, 197 (2019).